Photoacoustics 4 (2016) 112–123

Contents lists available at ScienceDirect

Photoacoustics

journal homepage: www.elsevier.com/locate/pacs

Review article

Photoacoustic imaging of the eye: A mini review

Wenzhong Liu[a], Hao F. Zhang[a,b,*]

[a] Department of Biomedical Engineering, Northwestern University, Evanston, IL 60208,USA
[b] Department of Ophthalmology, Northwestern University, Chicago, IL 60611, USA

ARTICLE INFO

Article history:
Received 15 January 2016
Received in revised form 15 April 2016
Accepted 17 May 2016
Available online 18 May 2016

Keywords:
Photoacoustic imaging
Eye
Diseases detection
Treatment monitoring
Medical tools

ABSTRACT

The eye relies on the synergistic cooperation of many different ocular components, including the cornea, crystalline lens, photoreceptors, and retinal neurons, to precisely sense visual information. Complications with a single ocular component can degrade vision and sometimes cause blindness. Immediate treatment and long-term monitoring are paramount to alleviate symptoms, restore vision, and cure ocular diseases. However, successful treatment requires understanding ocular pathological mechanisms, precisely detecting and monitoring the diseases. The investigation and diagnosis of ocular diseases require advanced medical tools. In this mini review, we discuss non-invasive photoacoustic (PA) imaging as a potential research tool and medical screening device. In the research setting, PA imaging can provide valuable information on the disease progression. In the clinical setting, PA imaging can potentially aid in disease detection and treatment monitoring.

Contents

1. Introduction and background

The eye is divided into the anterior and posterior segments (Fig. 1a) [1]. Prominent anterior segment structures include the cornea, iris, pupil, crystalline lens, and ciliary body. Prominent posterior segment structures include the vitreous body, retina,

* Corresponding author at: Department of Biomedical Engineering, Northwestern University, Evanston, IL 60208, USA.
E-mail address: hfzhang@northwestern.edu (H.F. Zhang).

http://dx.doi.org/10.1016/j.pacs.2016.05.001

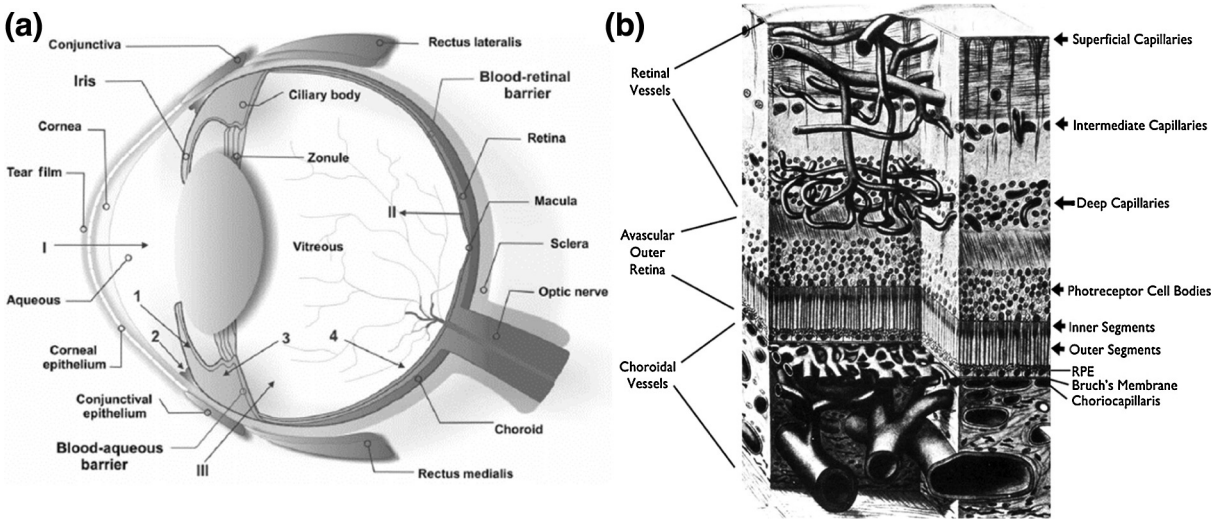

Fig. 1. (a) Schematic of normal ocular anatomy, I is anterior chamber, II is retinal pigment epithelium, III is vitreous. (b) Illustration of the retinal and choroidal vascular systems that nourish the retina in the posterior segment. RPE: retinal pigment epithelium.
Reprinted with permission from Refs. [1] and [5].

choroid, and optic nerve. All of these structures work together in a coordinated manner to provide visual information to the brain. However, before visual information is sent to the brain, it undergoes processing by structures in both the anterior and posterior segments. First, the cornea and lens form images on the retina [2], while the iris simultaneously adjusts pupil size to control the amount of light that reaches the retina. Second, retinal photoreceptors convert light into electrical signals [1], while pigment in the retinal pigment epithelium (RPE, mainly containing melanin) absorbs unnecessary light [3]. Third, retinal neurons modulate electrical signals and send them to brain for further processing.

Retinal and RPE processing of visual information consumes large amount of energy and oxygen [4]. Two delicate vascular circulation systems, the retinal and choroidal circulations, collectively support the retina (Fig. 1b) [5]. In a healthy eye, the retinal circulation mainly delivers oxygen and nutrients to the inner retinal tissues and the choroidal circulation mainly nourishes photoreceptors [6].

Eye diseases compromise, and even disable, normal functions of ocular components, which can threaten vision. Studies have demonstrated that variations in retinal blood oxygen saturation (sO_2) and RPE melanin concentration play an important role in several prevalent blinding ocular diseases. The sO_2 has been shown to be abnormal in diabetic retinopathy (DR) [7–9], glaucoma [10,11], and retinal venous occlusion [12,13]. Additionally, RPE melanin loss and lipofuscin accumulation have been shown to contribute to the progression of age-related macular degeneration (AMD) [14–16]. The ability to precisely detect aberrant retinal sO_2 values and RPE melanin concentrations can be important for improving investigations and diagnoses of ocular diseases.

In the past decades, large efforts have been made to quantitatively measure sO_2 and melanin concentration in the eye. Multi-wavelength fundus photography has been tested for a long time to measure retinal sO_2 [17–19] and has the advantage of being a non-contact technique. However, multi-wavelength fundus photographs often provide inaccurate measurements because of light scattering within retinal tissues and the RPE pigmentations [20]. Invasive methods, including fluorescence lifetime imaging and oxygen-sensitive microelectrode measurements, have been used to measure the partial pressure of oxygen in retinal tissue [21,22], but these methods are only suitable for laboratorial animal studies. Visible-light optical coherence tomography (vis-OCT) was recently used to successfully quantify retinal and choroidal sO_2 in rodents [23–25]. This non-contact technique has the benefits of accurately measuring sO_2 [26] and providing images with high depth resolution [23]. Therefore, vis-OCT has the potential to provide retinal and choroidal sO_2 measurements in the clinical setting. However, measurements made with vis-OCT have not yet been verified at many other different anatomical sites. This must be done before vis-OCT is tested in the clinical setting.

Measurements of RPE melanin have mostly been obtained during *in vitro* experiments. The most direct method to calculate melanin concentration involves manually counting melanin granules on high-magnification micrographs [27]. A less direct *in vitro* method involves measuring optical absorption of solubilized free melanin granules [28,29]. However, the invasive nature of these *in vitro* techniques prevents them from being used in clinical settings. Instead, spectroscopic fundus photography and near-infrared autofluorescence (NIR-AF) imaging are used to measure RPE melanin concentration *in vivo* [30–32]. Spectroscopic fundus photography uses mathematical optical models to estimate melanin optical density. However, over-simplified optical models used in spectral fundus photography calculations result in inaccurate melanin concentration measurements. The NIR-AF technique measures melanin concentration using the coincidence between the strong AF and NIR-excited melanin emission signals [32]. Unfortunately, a rigorous model that describes the relationship between AF and melanin has not yet been developed. Therefore, better non-invasive methods to measure retinal/choroidal blood sO_2 and RPE melanin concentration are still needed.

Blood and melanin both have high optical absorption coefficients within the visible light spectral range (Fig. 2) and optical absorption can be used to measure their concentrations [33]. Photoacoustic (PA) imaging has been shown to precisely and non-invasively measure optical absorption properties [34–40], and have already been used to measure both blood sO_2 and melanin concentration in the ear [41–44], brain [45,46], esophagus [47,48], colon [47,48], and epidermis (melanin only) [49,50]. Therefore, PA

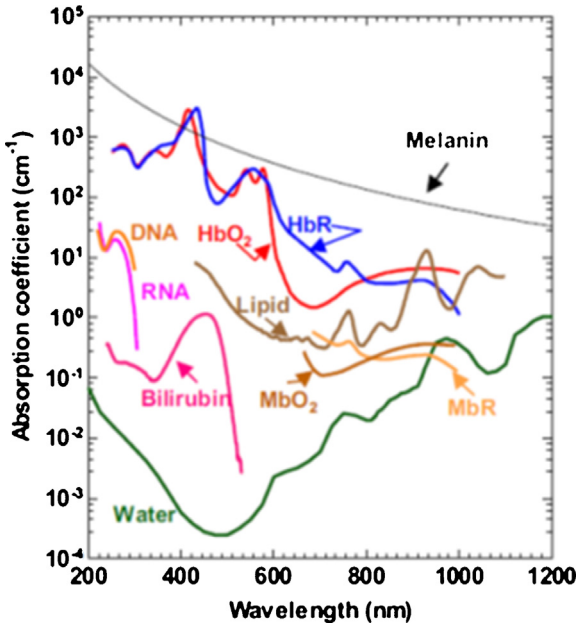

Fig. 2. Optical absorption spectra of blood components and melanin. HbR: deoxy-hemoglobin; HbO_2: oxy-hemoglobin; MbO_2: oxy-myoglobin; MbR: reduced myoglobin.
Reprinted with permission from Ref. [37].

imaging can potentially quantify retinal and choroidal sO_2 and the RPE melanin. In this mini review, we explain the principle of PA imaging, describe ocular imaging requirements, show PA images of the anterior and posterior ocular segments, and suggest areas of future research that will help bring PA imaging towards clinical ophthalmic applications.

2. Principles of photoacoustic imaging and requirements for imaging the eye

2.1. Principles of photoacoustic imaging

The principle of PA imaging has been previously described in other comprehensive reviews [34,35]; only the most essential steps are briefly described here. First, a laser is used to illuminate and excite the material being imaged. Short laser pulse illumination that satisfies both thermal and stress confinements is usually used to enhance the signal-to-noise ratio (SNR) of PA images [51]. Second, the sample being imaged absorbs some of the delivered laser energy, resulting in heat generation, transient thermoelastic expansion, and ultrasonic signal production. Third, the detected ultrasonic signals are used for both anatomical PA image reconstruction and functional analysis. For image reconstruction, single point laser excitation generates acoustic wave, which is recorded as a function of time. The time resolved PA signal is converted into one-dimensional depth-resolved image, referred to as A-line, based on the sound speed in tissue. A transverse linear scan of the point laser illumination on the sample yields a two-dimensional image by aligning A-lines according to theirs spatial locations, and a two-dimensional raster scan of the point illumination produces a three-dimensional image. For quantifications, the amplitude of the detected ultrasonic wave is proportional to the combination of molar extinction coefficient, the local optical-absorbing chromophore concentration, the local optical fluence, and the ultrasonic transducer response [52]. Chromophore concentration is generally the variable of interest and can be measured using PA images excited by multiple wavelengths (spectroscopic PA imaging), optical fluence modelling, and numerical analysis [35].

2.2. Ocular imaging requirements

The eye has several unique properties. It is a fragile organ and the photoreceptors are extremely sensitive to light that enters the eye [53]. The eye is always in motion [54] and the cornea and crystalline lens have their own optical powers, affecting how light is focused on the retina. Because of these properties, ocular imaging systems must meet several requirements. First, illumination intensity must be within safety limits. Over exposure can damage retina from three possible mechanisms, including thermal damage, thermoacoustic damage, and photochemical damage [55,56]. Different standards, such as International Commission on Non-Ionizing Radiation Protection (ICNIRP) broadband guidelines [57] and American National Standard for safe use of lasers (ANSI) [58], are available for guiding ophthalmic imaging safety. Among these different standards, recommended exposure limits are not substantially different. Almost all the reported PA ophthalmic imaging work evaluated their laser safeties according to the ANSI's criteria. Considering the combined effects of wavelength, exposure duration, repetition rate, illumination spot size, and pupil size and so on, ANSI determines ocular laser safety thresholds using the limits of maximum permissible exposure (MPE) for three types of illuminations: single pulse illumination (MPEsp), multiple pluses illumination (MPE_{MP}), and average power illumination (MPE_{GROUP}). The smallest value among MPE_{SP}, MPE_{MP}, and MPE_{GROUP} will be the safety limit. Detailed calculation of MPE_{SP}, MPE_{MP}, and MPE_{GROUP} can be found in ANSI. Second, noninvasive and noncontact imaging is highly preferred by both patients and physicians. Invasive imaging techniques carry the risk of numerous side effects, including, patient discomfort and nausea (from intravenous contrast agent). Third, high-speed imaging is preferred because the eye is always moving [59] and saccadic eye movements can cause motion artifacts, image blurring, and image distortion.

2.3. Measurements of optical absorption in the eye

Because of its high imaging resolution and non-invasiveness, optical absorption sensing attracts increasing attention in measuring RPE melanin concentration and retinal sO_2. The accuracy, however, depends on how to detect optical absorption, through either indirect or direct measurement. Indirect measurements acquire the fundus reflectance, and inversely calculate optical absorption within retinal blood and melanin based on numerical models such as Lambert-Beer's Law [60,61] or Radiative Transport Theory [62]. These numerical solutions, however, are sensitive to light scattering and local ocular geometrical parameters, such as retinal thickness, vessel diameters, and retinal pigmentation, thus may result in biased estimations. Taking retinal sO_2 quantification as an example, optical density (OD) needs to be estimated first as a measure of optical absorption. OD is defined as:

$$OD = \log_{10}\left(\frac{I_b}{I_v}\right), \tag{1}$$

where I_b is the reflection intensity from the vessel neighboring area, indicating the background reflectance; I_v is the reflection intensity directly from the vessel. In an ideal situation when photon path length within a vessel equals to the vessel diameter D, and the influences are negligible from light scattering in blood as well as photon absorption by melanin in I_v. Eq. (1) can be rewritten

as (details can be found in [20])

$$\begin{aligned} OD &= \log_{10}\left(\frac{I_b}{I_v}\right) \\ &= \log_{10}\left(e^{(\varepsilon_{HbO_2}(\lambda)\times[HbO_2]+\varepsilon_{HbR}(\lambda)\times[HbR])\times D}\right) + \log_{10}\left(e^{-\varepsilon_m(\lambda)\times C_m^{RPE}\times l}\right) \\ &= \frac{(\varepsilon_{HbO_2}(\lambda)\times[HbO_2]+\varepsilon_{HbR}(\lambda)\times[HbR])\times D}{\ln(10)} - \frac{\varepsilon_m(\lambda)\times C_m^{RPE}\times l}{\ln(10)} \end{aligned}, \tag{2}$$

where $\varepsilon_{HbO_2}(\lambda)$ and $\varepsilon_{HbO}(\lambda)$ are the molar extinction coefficients of oxygenated and deoxygenated hemoglobin; $[HbR]$ and $[HbO_2]$ are concentrations of the deoxygenated and oxygenated hemoglobin; l is the optical path length in the RPE; $C_m^{RPE}$is the melanin concentration in the RPE; $\varepsilon_m(\lambda)$ is the molar extinction coefficient of melanin at wavelength λ. From Eq. (2), the OD is underestimated because of the melanin in RPE, which in turn biases sO_2. In practice, the indirect measurement is, unfortunately, much more complex than the ideal case presented here. For example, the light scattering is strong within the vessel and the photon path length within the vessel will not be equal to vessel diameter D, which will further complicate optical absorption retrieve, and misestimate sO_2.

Compared with indirect measurement, directly measuring optical absorption with PA is more straightforward and can be more accurate. In PA imaging that satisfies requirements of thermal and stress confinements, the thermal expansion caused pressure rise P_0 is [34]

$$p_0 = \Gamma \times \mu_a \times F, \tag{3}$$

where Γ is *Gruneisen* coefficient; μ_a is the absorption coefficient; and F is the local optical fluence. Taking blood sO_2 imaging for example, the detected PA amplitude $pa(x,y,z,\lambda)$ is considered to be proportional to the local optical energy deposition $\phi(x,y,z,\lambda)$,

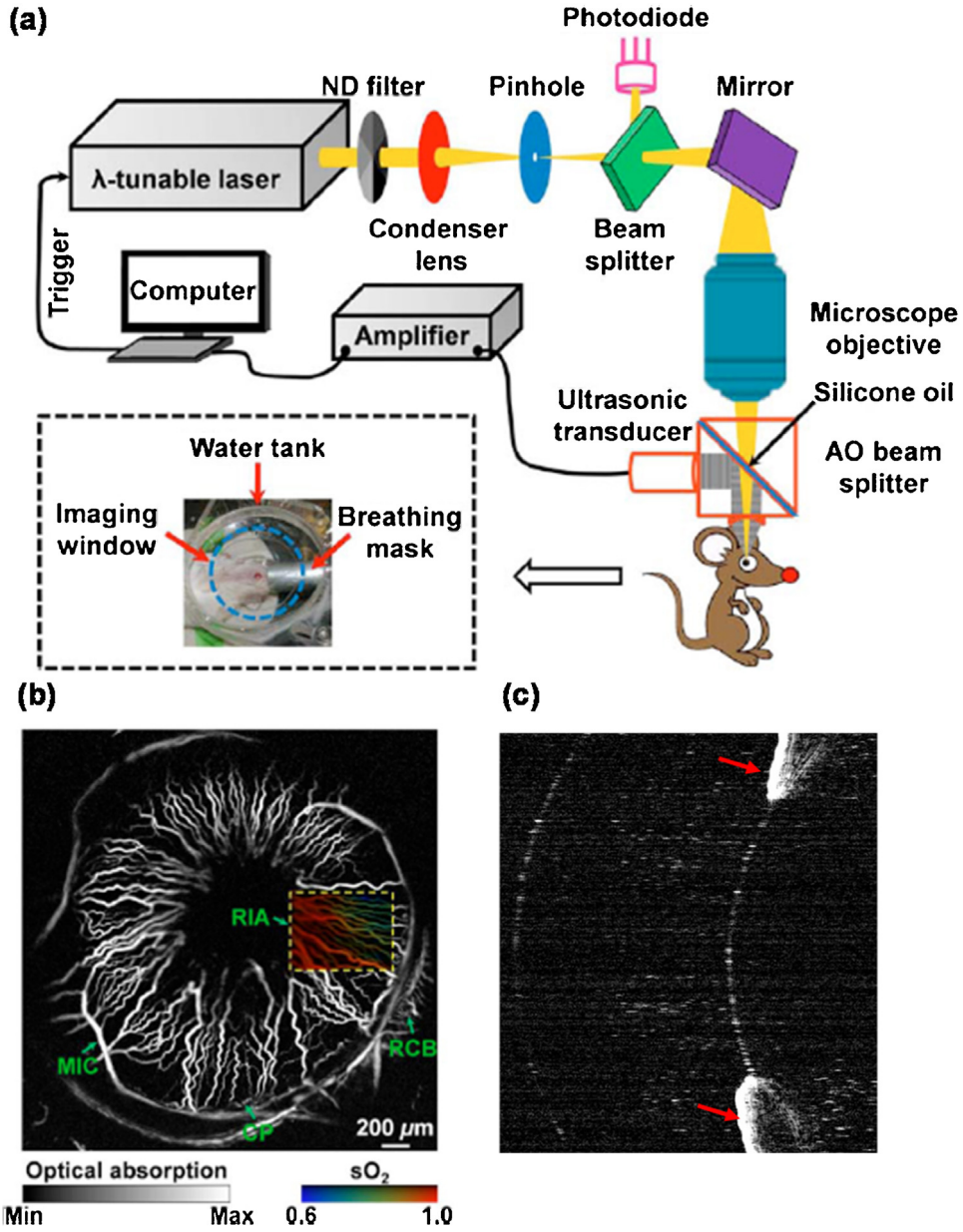

Fig. 3. (a) Schematic of a mechanical-scanning OR-PAM. (b) An in-vivo OR-PAM image of the iris microvasculature in an albino mouse. A false-colored map of the iris vasculature in the rectangular outlined area shows vessel sO_2. (c) A PA image showing iris melanin (red arrows) in an ex-vivo pig eye. ND: neutral density, AO: acoustic-optical, RIA: radial iris artery, MIC: major iris circle, RCB: recurrent choroidal branch, CP: ciliary process.
Reprinted with permission from Refs. [64] and [72].

which is a product of local absorption coefficient $\mu_a(x,y,z,\lambda)$ and local optical fluence $F(x,y,z,\lambda)$.

$$\begin{aligned} \mathrm{pa}(\lambda,x,y,z) &= K_1 \times \phi(\lambda,x,y,z) \\ &= K_1 \times F(x,y,z,\lambda) \\ &\times (\varepsilon_{HbR}(\lambda) \times [HbR] + \varepsilon_{HbO_2}(\lambda) \times [HbO_2]), \end{aligned} \quad (4)$$

where K_1 is the proportionality coefficient, reflecting the system sensitivity and *Gruneisen* coefficient. If we consider $F(x,y,z,\lambda)$ a constant, we can simplify $K_1 \times F(x,y,z,\lambda)$ as K_2. For multiple wavelength PA measurements, Eq. (4) becomes

$$\mathrm{PA} = K_2 \times M \times H, \quad (5)$$

where $M = \begin{bmatrix} \varepsilon_{HbR}(\lambda_1) & \varepsilon_{HbO_2}(\lambda_1) \\ \vdots & \vdots \\ \varepsilon_{HbR}(\lambda_n) & \varepsilon_{HbO_2}(\lambda_n) \end{bmatrix}$, $H = \begin{bmatrix} [HbR] \\ [HbO_2] \end{bmatrix}$, and $\mathrm{PA}(x,y,z) = \begin{bmatrix} \mathrm{pa}(\lambda_1,x,y,z) \\ \vdots \\ \mathrm{pa}(\lambda_n,x,y,z) \end{bmatrix}$

The sO_2 value of each vessel was then given by

$$sO_2(x,y,z) = \frac{[HbO_2]_{(x,y,z)}}{[HbO_2]_{(x,y,z)} + [HbR]_{(x,y,z)}}, \quad (6)$$

3. Photoacoustic imaging of the eye

Several groups developed PA imaging systems for the eye and reported ocular imaging since 2010 [63–65]. These ocular PA imaging systems can be classified into different categories. In terms of spatial resolution, there are acoustic-resolution and optical-resolution systems. Acoustic-resolution system weakly focuses excitation light onto ocular tissue, and the focus of the ultrasonic detector determines the imaging resolution [66,67]. Optical-resolution system tightly focuses the excitation light onto ocular tissue, where the optical focal spot determines the resolution [68]. PA imaging systems can also be categorized into mechanical-scanning and optical-scanning imaging systems. Mechanical-scanning PA imaging usually translates both the optical illumination and ultrasonic detection simultaneously for volumetric imaging [68]; while optical-scanning system employs a pair of galvanometers to scan a focused optical illumination and maintains the ultrasonic detection stationary [65,69].

Ocular PA imaging of both the anterior and posterior segments has been reported. In the early stages of development, researchers primarily used PA imaging to qualitatively examine ocular structures [63,65], including the iris and retinal vasculature. As PA imaging technology has advanced, more quantitative imaging has been the focus. This includes measurement of sO_2 [70] and retinal oxygen metabolic rate ($rMRO_2$) [71]. In this section, we summarize the development of ocular PA imaging of both anterior and posterior segment structures of the eye.

3.1. Anterior eye segment imaging

The major contrast of anterior segment PA imaging come from the red blood cells in the iris microvasculature and iris melanin. To image iris microvasculature and melanin, illumination light is directly focused on the iris. Both acoustic and optical resolution images were reported, but only a mechanical scanning system was used. de la Zerda et al. [63] qualitatively assessed the rabbit eye using acoustic resolution PA microscopy (AR-PAM). They successfully detected PA signals from the iris, but the iris microvasculature was not clearly visible in AR-PAM images because of the limited lateral resolution (approximately 200 μm). Mechanical-scanning optical resolution PA microscopy (OR-PAM) was used by Hu et al. [64] to obtain high resolution *in vivo* images of the iris microvascular in an albino mouse. Fig. 3a shows the OR-PAM system, in which a microscope objective lens (numerical aperture NA = 0.46) tightly focuses laser illumination light onto the iris microvasculature to achieve a lateral resolution of approximately 5 μm. Hu et al. [64] placed a water tank on top of the eye to relay ultrasonic signals from the iris to a focused 75 MHz ultrasonic detector (Fig. 3a). Fig. 3b shows the clearly visible iris microvasculature, where the diameter of a single capillary was estimated to be 6 μm. By using two excitation wavelengths (570 nm and 578 nm) with different oxy-hemoglobin and deoxy-hemoglobin absorption coefficients, Hu et al. [64] also quantitatively measured sO_2 of the iris microvasculature, as shown by the false-color map of the vasculature in Fig. 3b.

Iris melanin has also been measured using PA imaging. In an *ex vivo* pig eye experiment, Ronald et al. [72] used a mechanical scanning PA imaging system to image the iris melanin using both 1064-nm and 532-nm wavelength illuminations. An image obtained using the 532-nm light is shown in Fig. 3c. The authors observed strong PA signals from iris melanin with a 532 nm excitation light because melanin has a much larger absorption coefficient at 532 nm than it does at 1064 nm. Liu et al. [73] obtained *in vivo* images of mouse iris melanin using a mechanical-scanning OR-PAM system at an excitation wavelength of 532 nm. However, these melanin PA imaging studies only examined qualitative measures and, to date, quantitative measurements of iris melanin have not been obtained.

Imaging of anterior segment pathology with PAM has also been performed in *ex vivo* experiments and on wild-type rodents. Liu et al. [73] used a mechanical scanning OR-PAM to image corneal neovascularization in mice with alkali burns. In that study, a low-power objective lens (NA = 0.1) focused excitation light (523 nm)

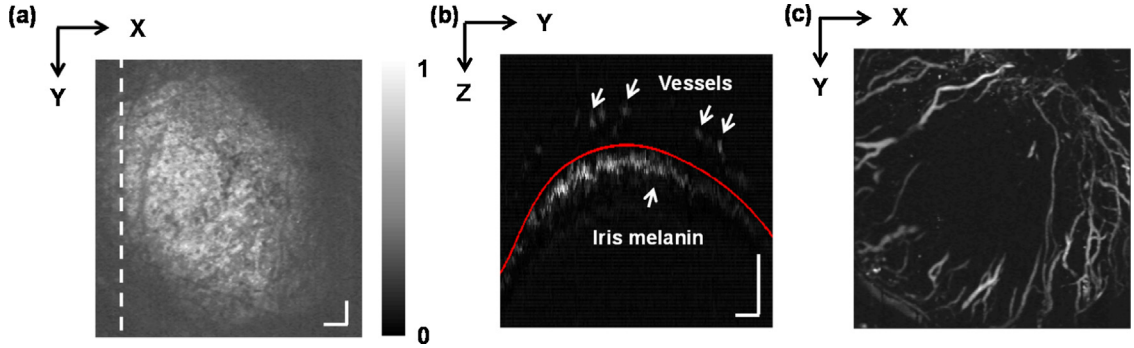

Fig. 4. OR-PAM imaging of mouse corneal vasculature in vivo. (a) Full-volume projection PAM image. (b) Cross-sectional PAM B-scan image taken along the dashed line in panel (a). The iris melanin (lower arrow) and corneal vessels (upper arrows) are clearly visible. (c) Corneal vasculature projection after segmentation of the corneal vasculature and iris melanin. Scale bar: 200 μm.
Reprinted with permission from Ref. [73].

onto the cornea to image the abnormal vasculature. Laser-induced ultrasonic signals were relayed to a focused ultrasonic detector (10 MHz) *via* a water tank that had been set on top of the cornea. Fig. 4a shows an *en face* projection PA imaging of the anterior eye segment, with signals from the cornea and iris being stacked together. Fig. 4b shows a PAM B-scan image of corneal vasculature and iris melanin. After segmentation of the cornea vasculature from iris melanin, a clear corneal vascular map was obtained (Fig. 4c).

Nearly all anterior segment PA images have been obtained with a mechanical scanning OR-PAM. However, there are concerns regarding mechanical-scanning OR-PAM imaging systems. First, mechanical scanning OR-PAM has a very limited imaging speed, where obtaining a 2 mm × 2 mm image can take more than 30 min [64]. Second, a water tank, usually placed on top of the eye, is needed to achieve ultrasonic coupling between the eye and the ultrasonic detector [64,73]. Therefore, these systems are not suitable for clinics, which requires fast imaging speeds and improved ultrasonic detection (as further discussed in Sections 3.2 and 4).

3.2. Posterior segment imaging

Posterior segment PA imaging of a normal eye images melanin in the RPE and red blood cells in the retinal and choroidal microvasculature. Both AR-PAM and OR-PAM systems have been used to obtain posterior segment images, along with mechanical scanning and optical scanning systems. de la Zerda et al. [63] demonstrated AR-PAM imaging of the retina and choroid in an *ex vivo* pig eye. Unfortunately, lateral image resolution was too low (around 200 μm) to visualize any features of the retinal or choroidal vasculature. To improve lateral resolution, Wu et al. [74] used OR-PAM imaging, which has a resolution of approximately 5 μm, to image the posterior segment in mice eyes. Although improved images of the retinal vasculature were obtained, the mechanical scanning caused a few concerns. First, as stated in Section 3.1, mechanical scanning PAM usually has low imaging speed and requires ultrasonic coupling between the eye and the ultrasonic transducer with a water tank. Additionally, for mechanical scanning OR-PAM imaging, laser-induced ultrasonic signals from the posterior segment must pass through the crystalline lens before reaching the ultrasonic transducer. Unfortunately, the lens strongly attenuates ultrasonic signals [75], which severely reduces the SNR of PA images. In experiments performed by Wu et al. [74] in mice, clear visualization of retinal vascular features was only achieved with an intense excitation laser power, which was above the ocular laser safety limit.

Jiao et al. [65] developed an optical-scanning PAM system, referred to as a photoacoustic ophthalmoscope (PAOM), to better image posterior segment [65,69]. In their PAOM system (Fig. 5a), a 532-nm pulse laser was used as the illumination source (pulse duration: 2 ns; pulse repetition rate: 30 kHz), with output pulse laser light coupled to a 1 × 2 single-mode optical fiber. One output was used for compensating for laser intensity variation; the other was the excitation source, which was steered by a pair of galvanometer mirrors and relayed to the cornea by a pair of telescope lenses [65]. Laser-induced PA waves from the posterior segment were detected by a custom-built needle ultrasonic transducer (center wavelength: 30 MHz; bandwidth: 50%; active element diameter: 1 mm), which was placed in contact with the eyelid and coupled by ultrasound gel (Fig. 5b). The lateral and axial resolution of PA images was approximately 20 and 23 μm, respectively. PAOM has several advantages over mechanical-scanning OR-PAM. First, PAOM's imaging speed (up to 30 kHz) is much faster than that of any mechanical-scanning OR-PAM. Second, there is no need to place a water tank on top of the eye to achieve ultrasonic coupling. Instead, an ultrasonic needle transducer is directly coupled to the eyelid. Third, the needle transducer in PAOM detects most ultrasonic signals propagating from vitreous humor to eyelid, which prevents strong ultrasonic signals attenuation from lens and enables high SNR imaging. Several studies have successfully used PAOM to obtain high quality images of the retinal vasculature, the choroidal vasculature, and RPE melanin in rodents (Fig. 6) [69,76–81].

Multi-modal imaging can be very beneficial for investigating ocular pathological and detecting disease [82,83]. For the readers' convenience, we briefly summarize merits and concerns of different ophthalmic imaging devices in Table 1, including OCT, confocal scanning laser ophthalmoscopy (cSLO), fundus photography, hyperspectral imaging (HSI), and PAOM.

When PAOM is integrated with other imaging modalities, more structural and functional information can be obtained. For example, integrating PAOM and auto-florescence imaging can provide information on the retinal vasculature and on the distribution and concentration of retinal melanin and lipofuscin [76]. Combining multi-wavelength PAOM and fluorescein

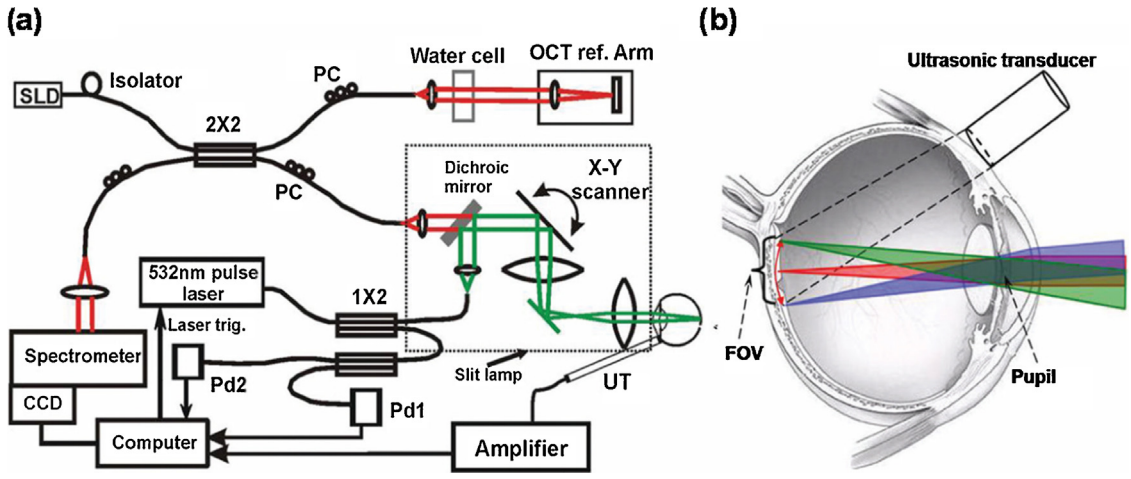

Fig. 5. (a) An optical scanning PAOM combined with OCT. (b) Illustration of ultrasonic transducer position and how the optical illumination beam enters the eye and focuses on the retina. SLD: superluminescent diode, OCT: optical coherence tomography, PC: polarization controller, CCD: charge coupled device, Pd: photodiode, UT ultrasonic transducer, FOV: field of view.
Reprinted with permission from Ref. [65].

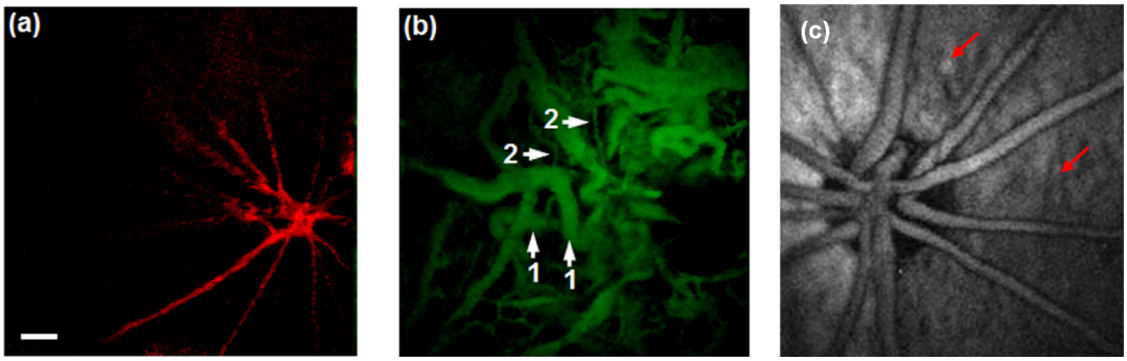

Fig. 6. (a) PAOM imaging of retinal vasculature in an albino mouse. (b) PAOM imaging of choroidal vasculature in an albino mouse; 1 major choroidal vessels, 2 small choroidal vessels. (c) PAOM imaging of retinal pigment epithelium melanin (red arrows) and the retinal vasculature in a pigmented rat. Scale bar: 100 μm. Fig. 6 (a) and (b). Reprinted with permission from Ref. [81].

Table 1
Summary of ophthalmic imaging devices.

Technology	Technique requirements	Applications	Advantages	Concerns
OCT [23,123–125]	Broadband illumination, interferometer based sensing, confocal detection, optical scanning	Intra-retinal layer structures, angiography, blood flow, sO_2, birefringence	High depth and lateral resolution, non-contact sensing of multi-parameters	Limited field of view in angiography, artifacts in flow and birefringence imaging, human retinal sO_2 is not reported yet.
cSLO [126,127]	Narrowband/single wavelength illumination, confocal detection, optical scanning	Retinal fundus structures, fluorescein angiography, sO_2, auto-fluorescence	High lateral resolution, fast imaging	Poor depth resolution , measurement of sO_2 is influenced by light scattering, angiography requires contrast agents
Fundus Photography [18,128,129]	Flood illumination	Retinal fundus structures, fluorescein angiography, sO_2, auto-fluorescence	Non optical scanning, fast imaging,	Non-depth resolution , measurement of sO_2 is influenced by light scattering, angiography requires contrast agents, speckle noise, aberrations
HSI [130,131]	Broadband illumination, Flood illumination	Retinal fundus structures, sO_2, macular pigment	Non optical scanning Spectroscopic analysis	Slow imaging, non-depth resolution, measurement of sO_2 and pigment are influenced by light scattering
PAOM [65,71]	Pulse laser excitation, acoustic signals detection, optical scanning	Angiography, sO_2 and pigment imaging	Moderate depth resolution, pure optical absorption sensing	Image only optical absorption, require “contact” detection

angiography [69] can measure retinal blood sO_2 and map the retinal and choroidal vasculature. The most useful integrated imaging system utilizes both multi-wavelength PAOM and OCT (Fig. 5a), which has several advantages. OCT can provide both structural and functional information of the posterior segment. With broadband illumination, OCT can detail 3D retinal and choroidal structural information with high axial and lateral resolutions [84,85]. Using repeated scanning, OCT can achieve complete retinal vasculature mapping [86–88]. By detecting Doppler phase shifts caused by moving blood, OCT can quantitatively measure retinal blood velocity and flow rate [89–91]. Implementation of polarization sensitive OCT [92–94], retinal birefringence can be retrieved. Besides aforementioned advantages, OCT can also guide PAOM imaging, allowing PAOM to image a specific region of interest in the posterior segment [95]. Multi-wavelength PAOM can quantify retinal sO_2 and has the potential to measure RPE melanin concentration [96]. Recently, Wei and Liu et al. [71,97] successfully measured $rMRO_2$ in rats using an integrated PAOM and OCT system. Retinal sO_2 was calculated using PAOM measurements at three wavelengths (570 nm, 578 nm, and 588 nm; Fig. 7b), and blood flow rate was quantified by the near infrared Doppler OCT (NIR-OCT) (center wavelength: 850 nm; bandwidth: 50 nm; Fig. 7e). For our readers' convenience, we summarize the reported ocular PA imaging systems in Table 2.

4. Future studies to bring photoacoustic imaging to the clinical setting

This section focuses on investigations that can potentially facilitate the beginning clinical trials with PA ocular imaging systems.

4.1. Technique development

4.1.1. Non-contact detection of photoacoustic signals

As already stated in Section 3.1, a major concern about current ocular PA imaging systems is the requirement of physical contact between the eye and the ultrasonic detector. In reported works, researchers either placed a water tank above the cornea or directly coupled an ultrasonic needle transducer with the eyelid using ultrasonic gel [71]. However, these methods are not ideal for the clinical settings. Detection methods that require contact with the eye generally cause patient discomfort. Additionally, physical motion from eye saccades and head movements can affect

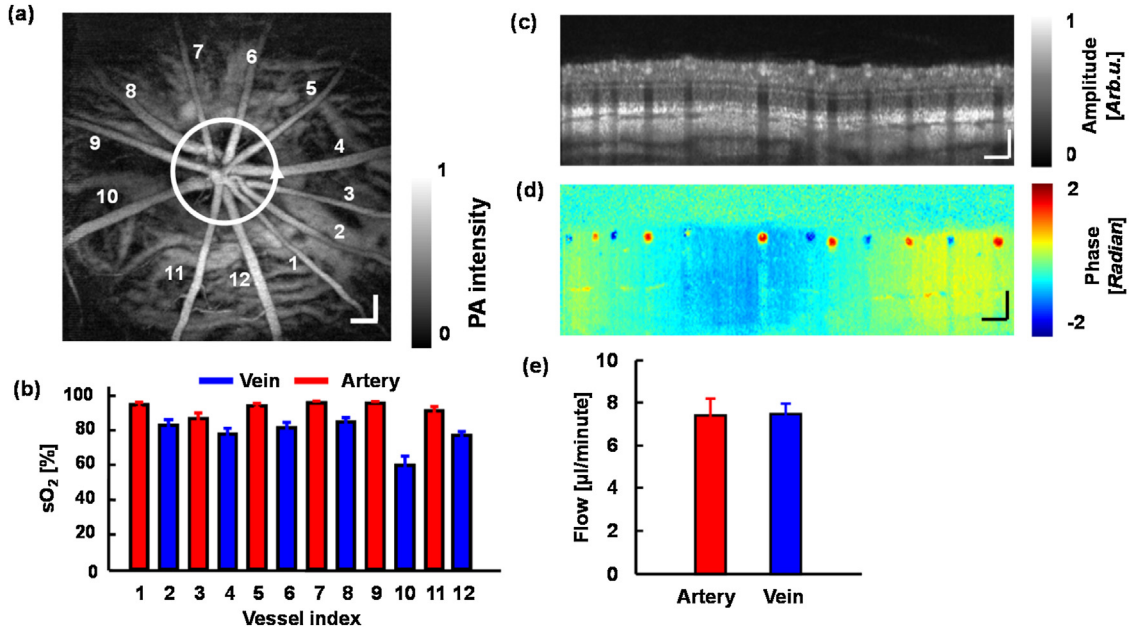

Fig. 7. Retinal oxygen metabolic rate was measured using integrated PAOM and OCT. (a) Image of the retinal and choroidal vasculature obtained with PAOM at 570 nm. (b) Calculated oxygen saturation (sO_2) values in the major retinal vessels. (c) Cross-sectional OCT B-scan image obtained along the white circle in (a). (d) OCT phase shift B-scan image taken along the white circle in (a). (e) Measured flow rate in the retinal arterial and venous systems. Scale bars: 200 μm.
Reprinted with permission from Ref. [71].

Table 2
Summary of reported photoacoustic imaging of eye.

Reported system	Scanning pattern	Reported imaging speed and imaging size	Reported resolution	Reported Laser illumination	Reported Laser safety evaluation	Applications
Zerda et al. [63] (*Both in vivo and ex vivo study*)	Wide filed illumination	90 min for 12 mm × 8 mm	Axial: 50/83 μm Lateral: 200/240 μm	Wavelength: 740 nm Pulse energy density: 0.5 mJ/cm^2	Safe (Based on ANSI 2000)	Both anterior and posterior segment
Hu et al. [64] (*in vivo study*)	Mechanical scanning	120 min for 2 mm × 2 mm	Axial: 15 μm Lateral: 5 μm	Wavelength: 570/578 nm Pulse energy: 40 nJ	Safe (Based on ANSI 2007)	Anterior segment
Liu et al. [73] (*in vivo study*)	Mechanical scanning	20 min for 3 mm × 3 mm	Axial: 50 μm Lateral: 2.76 μm	Wavelength: 532 nm Pulse energy: 80 nJ	Safe (Based on ANSI 2007)	Anterior segment
Silverman et al. [72] (*ex vivo study*)	Mechanical scanning	Not mentioned	Axial: 37 μm Lateral: 20 μm	Wavelength: 532/1064 nm Pulse energy: 1 μJ	Not Safe (Based on ANSI 2007)	Both anterior and posterior segment
Wu et al. [74] (*In vivo study*)	Mechanical scanning	6.5 min for 2 mm × 2 mm	Axial: 45 μm Lateral: 5 μm	Wavelength: 532 nm Pulse energy: 500 nJ	Not Safe (Based on ANSI 2007)	Both anterior and posterior segment
Jiao et al. [65] (*In vivo study*)	Optical scanning	2.7 s for 2 mm × 2 mm	Axial: 23 μm Lateral: 20 μm	Wavelength: 532 nm Pulse energy: 40 nJ	Safe (Based on ANSI 2007)	Posterior segment
Song et al. [69] (*In vivo study*)	Optical scanning	2.7 s for 2 mm × 2 mm	Axial: 23 μm Lateral: 20 μm	Wavelength: 532 nm Pulse energy: 40 nJ	Safe (Based on ANSI 2007)	Posterior segment
Song et al. [71] (*In vivo study*)	Optical scanning	2.7 s for 2 mm × 2 mm	Axial: 23 μm Lateral: 20 μm	Wavelength: 570/578/588 nm Pulse energy: 40 nJ	Safe (Based on ANSI 2007)	Posterior segment
Liu et al. [77] (*In vivo study*)	Optical scanning	2.7 s for 2 mm × 2 mm	Axial: 23 μm Lateral: 20 μm	Wavelength: 532 nm Pulse energy: 60 nJ	Safe (Based on ANSI 2007)	Posterior segment

coupling between ultrasonic transducer and eyeball, and influence PA image SNR. Lastly, current ultrasonic coupling methods are not ideal. When a water tank is used for ultrasonic coupling, integration of PA and other imaging modalities becomes difficult. When using direct coupling between a needle detector and the eyelid, a long working distance is required. This forces the objective to have a very small NA for PA imaging systems and other integrated imaging modalities like OCT.

Novel detection methods are needed to overcome these issues and many are already under investigation. Some researchers have studied wearable, transparent ultrasonic detectors that can be fitted to clinical ocular PA imaging devices. Zhang group [98–100] developed a small-footprint, optically transparent, micro-ring resonator to detect ultrasonic signals (diameter of a few millimetres). The micro-ring resonator has a lower noise equivalent pressure [98] than other ultrasonic detectors. These properties

make it feasible for this transducer to be fabricated into a contact lens, which can serve as an ultrasonic detector for ocular PA imaging. Even though the contact lens is still a contact detector, it does not require ultrasonic gel for coupling and allows for a flexible working distance, which will reduce patient discomfort as well as facilitate integration of PA imaging with other imaging modalities.

Other non-contact ultrasonic detectors have been also extensively studied. Several groups used interferometer to sense surface displacement induced by laser excitation [101–105] in preliminary experiments. Sampathkumar and Silverman [106] used a Michelson interferometer to detect PA signals in *ex vivo* porcine eyes. Chen et al. [107] used an OCT to detect *in vivo* PA signals in a mouse ear. Rousseau et al. [104] detected PA signals using a Fabry-Perot interferometer on a chicken breast tissue sample. Unfortunately, concerns about all reported non-contact ultrasonic detection methods include performance stability and detection sensitivity [98]. Future studies are needed so that better non-contact PA methods can be discovered.

4.1.2. Development of innovative laser sources for photoacoustic ophthalmic imaging

Suitable laser sources of PAOM will need to have a short pulse duration (for example, 10 ns or shorter), sufficient pulse energy (for example, 40 nJ) and high repetition rate. Qualified eye anatomical images are achievable with monochromatic pulse laser illumination. Liu et al. [73] employed a single wavelength Nd:YAG pulse laser (532 nm wavelength, 1 ns pulse duration, 80 nJ pulse energy, and 1 kHz pulse repetition rate) to image corneal neovascularization structures. Zerda et al. [63] applied Na:YAG laser combined with an optical parametric oscillator (OPO) modulator (740 nm wavelength, 5 ns pulse duration, 0.5 mJ/cm^2 fluence rate) to image the whole eye structures. Using PAOM to resolve ocular functional information requires multi-wavelength laser illuminations. Hu et al. [64] used a tunable pulse dye laser at two wavelengths (570 nm and 578 nm) to measure iris vascular sO_2; Song et al. [71] also recruited a tunable pulse dye laser at three wavelengths (578 nm, 580 nm, 588 nm) to quantify retinal sO_2. To access multimodal information, PAOM is usually integrated with other imaging modalities, for instance, OCT. The integrated PAOM and OCT, however, require different types of illuminations, and thus demand separate light sources [71], which is inconvenient. A single laser source that allows both PA imaging and OCT was recently investigated. With phantom experiments, Lee et al. [108] shown that a near-infrared supercontinuum laser can allow both PA and OCT imaging. Recently, Liu et al. [109] successfully acquired *in vivo* rat retinal images from simultaneous PAOM and OCT by using a single ultrafast laser source (center wavelength 800 nm, bandwidth 30 nm, pulse duration 3 ns, repetition rate 10 kHz). To further develop a compact and cost-effective PA imaging system, researchers have also developed pulse laser diodes (PLDs) as alternative laser excitation sources [110,111], and mouse ear vascular structures were successfully obtained. Ophthalmic applications of PLDs are not reported yet and are still under investigation.

4.1.3. Imaging depth, resolution and speed of photoacoustic ophthalmoscopy

An optimal PAOM system requires the extended imaging depth to cover both retina and choroid, high lateral and axial resolutions to resolve RPE melanin, and fast imaging speed to circumvent motion artifacts. For imaging depth, application of optical clearing agents can reduce tissue scattering influences and allow deep imaging [112], which, however, is not suitable for *in vivo* ocular using. Near-infrared light (NIR) PAM can image much deeper than visible light [113], the required high power excitation in NIR is a potential safety concern. Besides, sO_2 measurement may be difficult with NIR illumination. The lateral imaging resolution of PAOM is limited to around 20 μm in rodent eyes, which is not enough to resolve retinal capillaries. The low lateral resolutions of PAOM result from a narrow laser beam used, which aims to reduce influence of aberration from ocular lens. To improve the lateral resolution, the synthetic-aperture technique can potentially be implemented in PAOM [114,115]. The axial resolution of PAOM is determined by the bandwidth of the ultrasonic transducer and larger ultrasonic bandwidth will allow higher axial resolution. However, a transducer with large bandwidth needs to be carefully chosen. Due to ocular attenuation of high frequency ultrasonic waves, it's suggested that high sensitivity in PAOM is more achievable with relative narrow bandwidth [116]. Therefore, the tradeoff between axial resolution and detection sensitivity needs a balance. For imaging speed, it can still be improved, depending on laser repetition rate, until it is limited by the ultrasound propagation time from the posterior eye. High imaging speed will reduce the influence of eyeball motion on image quality.

4.1.4. Exogenous contrast agents for photoacoustic ophthalmic imaging

Exogenous contrast agents are widely used in PA imaging to improve photoacoustic imaging quality [38,117], and to extend the imaging scopes to molecular and genetic imaging [118]. Despite not being used in ocular PA imaging yet, some of the common adopted ophthalmic contrast agents were already tested on other anatomic sites and achieved enhanced results. These exogenous agents will have great potential to improve/extend PA ophthalmic applications. We summarize the common used ophthalmic contrast agents in Table 3.

4.2. Photoacoustic imaging of animal eyes

Before clinical adaptation, ocular PA imaging requires numerous animal studies to verify the longitudinal performance stability of ocular PA measurements. Also, better understanding of early disease activity is important to apply PA imaging for ocular diseases detection. For example, knowing how early can PA detect retinal sO_2 changes in DR would be helpful in determining when to begin screening diabetic patients with the technology. Lastly, visual stimuli can cause neurovascular coupling in the retina, and have been reported to change retinal vessel diameter, blood flow, and retinal sO_2 [119–121]. The reported visual stimulus had a flicker frequency between 10 Hz and 60 Hz, with a stimulation time

Table 3
Summary of common ophthalmic contrast agents for photoacoustic imaging.

Contrast agents	Benefits and Applications	Concerns
Evans blue [132]	Complete and continuous microvascular network mapping	Photobleaching of Evans blue
Indocyanine green (ICG) [133,134]	Near-infrared photoacoustic imaging, high penetration depth	Rapid circulation and clearance from bloodstream
Nanoparticles [135]	Near-infrared photoacoustic imaging, high penetration depth; biomarkers for molecular imaging; relative slow tissue clearance.	Safety issue

greater than 10 s [122]. These stimuli are vastly different from the visible light that is used for illumination in PAOM, which has a repeat frequency of up to several kilohertz. Still, studies examining how visible light illumination influences PAOM accuracy are needed.

5. Summary

This mini review briefly introduced ocular physiology, described prevalent ocular diseases that cause blindness, and summarized evidence of aberrant retinal sO_2 and RPE melanin concentration in these blinding diseases. We also described recent efforts to measure retinal sO_2 and RPE melanin concentration and discussed how PA imaging allows for the precise quantification of these parameters. We summarized recent developments in PA imaging that have improved both anterior and posterior segment imaging, and discussed potential areas of research that will facilitate adopting ocular PA imaging in the clinical setting.

Conflict of interest

Hao F. Zhang has financial interest in Opticent Inc., which, however, did not support any work in this review. Wenzhong Liu has no conflict of interest.

Acknowledgements

The authors would like to thank Dr. Hao Li and Dr. Biqin Dong for fruitful discussions. This work was supported by NIH grants 1R01EY019951, 1R24EY022883, and 1DP3DK108248; and NSF grants CBET-1055379 and DBI-1353952. Wenzhong Liu is supported by the International Graduate Research Fellowship from the Howard Hughes Medical Institute.

References

[1] C.E. Willoughby, D. Ponzin, S. Ferrari, A. Lobo, K. Landau, Y. Omidi, Anatomy and physiology of the human eye: effects of mucopolysaccharidoses disease on structure and function—a review, Clin. Exp. Ophthalmol. 38 (2010) 2–11.
[2] P. Artal, A. Benito, J. Tabernero, The human eye is an example of robust optical design, J. Vis. 6 (2006) 1–1.
[3] B. Winn, D. Whitaker, D.B. Elliott, N.J. Phillips, Factors affecting light-adapted pupil size in normal human subjects, Invest. Ophthalmol. Vis. Sci. 35 (1994) 1132–1137.
[4] D.-Y. Yu, S.J. Cringle, Oxygen distribution and consumption within the retina in vascularised and avascular retinas and in animal models of retinal disease, Prog. Retin. Eye Res. 20 (2001) 175–208.
[5] P.A. Campochiaro, Molecular pathogenesis of retinal and choroidal vascular diseases, Prog. Retin. Eye Res. 49 (2015) 67–81.
[6] C. Delaey, J. van de Voorde, Regulatory mechanisms in the retinal and choroidal circulation, Ophthal. Res. 32 (2000) 249–256.
[7] B. Khoobehi, K. Firn, H. Thompson, M. Reinoso, J. Beach, Retinal arterial and venous oxygen saturation is altered in diabetic patientsretinal oxygen saturation trend in diabetes, Invest. Ophthalmol. Vis. Sci. 54 (2013) 7103–7106.
[8] S.H. Hardarson, E. Stefansson, Retinal oxygen saturation is altered in diabetic retinopathy, Br. J. Ophthalmol. 96 (2012) 560–563.
[9] M. Hammer, W. Vilser, T. Riemer, A. Mandecka, D. Schweitzer, U. Kuhn, J. Dawczynski, F. Liemt, J. Strobel, Diabetic patients with retinopathy show increased retinal venous oxygen saturation, Graefes Arch. Clin. Exp. Ophthalmol. 247 (2009) 1025–1030.
[10] O.B. Olafsdottir, S.H. Hardarson, M.S. Gottfredsdottir, A. Harris, E. Stefánsson, Retinal oximetry in primary open-angle glaucoma, Invest. Ophthalmol. Vis. Sci. 52 (2011) 6409–6413.
[11] E. Vandewalle, L. Abegão Pinto, O.B. Olafsdottir, E. De Clerck, P. Stalmans, J. Van Calster, T. Zeyen, E. Stefánsson, I. Stalmans, Oximetry in glaucoma: correlation of metabolic change with structural and functional damage, Acta Ophthalmol. (Copenh.) 92 (2014) 105–110.
[12] S.H. Hardarson, E. Stefánsson, Oxygen saturation in central retinal vein occlusion, Am. J. Ophthalmol. 150 (2010) 871–875.
[13] T. Eliasdottir, D. Bragason, S. Hardarson, E. Stefánsson, Retinal oxygen saturation is affected in central retinal vein occlusion, Invest. Ophthalmol. Vis. Sci. 54 (2013) 46–46.
[14] T.T. Berendschot, R.A. Goldbohm, W.A. Klopping, J. van de Kraats, J. van Norel, D. van Norren, Influence of lutein supplementation on macular pigment, assessed with two objective techniques, Invest. Ophthalmol. Vis. Sci. 41 (2000) 3322–3326.
[15] J.T. Landrum, R.A. Bone, M.D. Kilburn, The macular pigment: a possible role in protection from age-related macular degeneration, Adv. Pharmacol. 38 (1997) 537–556.
[16] L.G. Hyman, A.M. Lilienfeld, F.L. Ferris, 3rd, and S. L. Fine, Senile macular degeneration: a case-control study, Am. J. Epidemiol. 118 (1983) 213–227.
[17] J.C. Ramella-Roman, S.A. Mathews, H. Kandimalla, A. Nabili, D.D. Duncan, S.A. D'Anna, S.M. Shah, Q.D. Nguyen, Measurement of oxygen saturation in the retina with a spectroscopic sensitive multi aperture camera, Opt. Express 16 (2008) 6170–6182.
[18] A. Harris, R.B. Dinn, L. Kagemann, E. Rechtman, A review of methods for human retinal oximetry, Ophthal. Surg. Lasers Imaging 34 (2003) 152–164.
[19] D. Schweitzer, M. Hammer, J. Kraft, E. Thamm, E. Konigsdorffer, J. Strobel, In vivo measurement of the oxygen saturation of retinal vessels in healthy volunteers, IEEE Trans. Biomed. Eng. 46 (1999) 1454–1465.
[20] W. Liu, S. Jiao, H.F. Zhang, Accuracy of retinal oximetry: a Monte Carlo investigation, J. Biomed. Opt. 18 (2013) 066003.
[21] R. Shonat, A. Kight, Oxygen tension imaging in the mouse retina, Ann. Biomed. Eng. 31 (2003) 1084–1096.
[22] N.D. Wangsa-Wirawan, R.A. Linsenmeier, Retinal oxygen: fundamental and clinical aspects, Arch. Ophthalmol. 121 (2003) 547–557.
[23] J. Yi, Q. Wei, W. Liu, V. Backman, H.F. Zhang, Visible-light optical coherence tomography for retinal oximetry, Opt. Lett. 38 (2013) 1796–1798.
[24] S. Chen, J. Yi, H.F. Zhang, Measuring oxygen saturation in retinal and choroidal circulations in rats using visible light optical coherence tomography angiography, Biomed. Opt. Express 6 (2015) 2840–2853.
[25] S.P. Chong, C.W. Merkle, C. Leahy, H. Radhakrishnan, V.J. Srinivasan, Quantitative microvascular hemoglobin mapping using visible light spectroscopic Optical Coherence Tomography, Biomed. Opt. Express 6 (2015) 1429–1450.
[26] S. Chen, J. Yi, W. Liu, V. Backman, H.F. Zhang, Monte Carlo investigation of optical coherence tomography retinal oximetry, IEEE Trans. Biomed. Eng. 62 (2015) 2308–2315.
[27] L. Feeney-Burns, E.S. Hilderbrand, S. Eldridge, Aging human RPE: morphometric analysis of macular, equatorial, and peripheral cells, Invest. Ophthalmol. Vis. Sci. 25 (1984) 195–200.
[28] J.J. Weiter, F.C. Delori, G.L. Wing, K.A. Fitch, Retinal pigment epithelial lipofuscin and melanin and choroidal melanin in human eyes, Invest. Ophthalmol. Vis. Sci. 27 (1986) 145–152.
[29] S.Y. Schmidt, R.D. Peisch, Melanin concentration in normal human retinal pigment epithelium. Regional variation and age-related reduction, Invest. Ophthalmol. Vis. Sci. 27 (1986) 1063–1067.
[30] M.J. Kanis, T.T. Berendschot, D. van Norren, Influence of macular pigment and melanin on incident early AMD in a white population, Graefes Arch. Clin. Exp. Ophthalmol. 245 (2007) 767–773.
[31] T.T. Berendschot, J.J. Willemse-Assink, M. Bastiaanse, P.T. de Jong, D. van Norren, Macular pigment and melanin in age-related maculopathy in a general population, Invest. Ophthalmol. Vis. Sci. 43 (2002) 1928–1932.
[32] C.N. Keilhauer, F.C. Delori, Near-infrared autofluorescence imaging of the fundus: visualization of ocular melanin, Invest. Ophthalmol. Vis. Sci. 47 (2006) 3556–3564.
[33] L.J. Steven, Optical properties of biological tissues: a review, Phys. Med. Biol. 58 (2013) R37.
[34] M. Xu, L.V. Wang, Photoacoustic imaging in biomedicine, Rev. Sci. Instrum. 77 (2006) 041101.
[35] B. Cox, J.G. Laufer, S.R. Arridge, P.C. Beard, Quantitative spectroscopic photoacoustic imaging: a review, J. Biomed. Opt. 17 (2012) 0612021–06120222.
[36] L.V. Wang, Multiscale photoacoustic microscopy and computed tomography, Nat. Photon. 3 (2009) 503–509.
[37] J. Yao, L.V. Wang, Sensitivity of photoacoustic microscopy, Photoacoustics 2 (2014) 87–101.
[38] L.V. Wang, S. Hu, Photoacoustic tomography: in vivo imaging from organelles to organs, Science 335 (2012) 1458–1462.
[39] A.P. Jathoul, J. Laufer, O. Ogunlade, B. Treeby, B. Cox, E. Zhang, P. Johnson, A.R. Pizzey, B. Philip, T. Marafioti, M.F. Lythgoe, R.B. Pedley, M.A. Pule, P. Beard, Deep in vivo photoacoustic imaging of mammalian tissues using a tyrosinase-based genetic reporter, Nat. Photon. 9 (2015) 239–246 (Advance Online Publication).
[40] H.F. Zhang, K. Maslov, G. Stoica, L.V. Wang, Functional photoacoustic microscopy for high-resolution and noninvasive in vivo imaging, Nat. Biotechnol. 24 (2006) 848–851.
[41] J. Yao, K.I. Maslov, Y. Zhang, Y. Xia, L.V. Wang, Label-free oxygen-metabolic photoacoustic microscopy in vivo, J. Biomed. Opt. 16 (2011) (076003-076003-076011).
[42] S. Hu, K. Maslov, L.V. Wang, Second-generation optical-resolution photoacoustic microscopy with improved sensitivity and speed, Opt. Lett. 36 (2011) 1134–1136.
[43] A. Krumholz, L. Wang, J. Yao, L.V. Wang, Functional photoacoustic microscopy of diabetic vasculature, J. Biomed. Opt. 17 (2012) 060502.
[44] B. Ning, M.J. Kennedy, A.J. Dixon, N. Sun, R. Cao, B.T. Soetikno, R. Chen, Q. Zhou, K. Kirk Shung, J.A. Hossack, S. Hu, Simultaneous photoacoustic microscopy of microvascular anatomy oxygen saturation, and blood flow, Opt. Lett. 40 (2015) 910–913.

[45] S. Hu, K. Maslov, V. Tsytsarev, L.V. Wang, Functional transcranial brain imaging by optical-resolution photoacoustic microscopy, J. Biomed. Opt. 14 (2009) 040503–040503.
[46] J. Yao, L. Wang, J.-M. Yang, K.I. Maslov, T.T.W. Wong, L. Li, C.-H. Huang, J. Zou, L. V. Wang, High-speed label-free functional photoacoustic microscopy of mouse brain in action, Nat. Methods 12 (2015) 407–410.
[47] J.-M. Yang, C. Favazza, R. Chen, J. Yao, X. Cai, K. Maslov, Q. Zhou, K.K. Shung, L. V. Wang, Simultaneous functional photoacoustic and ultrasonic endoscopy of internal organs in vivo, Nat. Med. 18 (2012) 1297–1302.
[48] T.-J. Yoon, Y.-S. Cho, Recent advances in photoacoustic endoscopy, World J. Gastrointest. Endosc. 5 (2013) 534–539.
[49] J.T. Oh, M.L. Li, H.F. Zhang, K. Maslov, G. Stoica, L.V. Wang, Three-dimensional imaging of skin melanoma in vivo by dual-wavelength photoacoustic microscopy, J. Biomed. Opt. 11 (2006) 34032.
[50] J.A. Viator, J. Komadina, L.O. Svaasand, G. Aguilar, B. Choi, J. Stuart Nelson, A comparative study of photoacoustic and reflectance methods for determination of epidermal melanin content, J. Invest. Dermatol. 122 (2004) 1432–1439.
[51] J. Xia, J. Yao, L.V. Wang, Photoacoustic tomography: principles and advances, Electromagn. Waves (Cambridge, Mass.) 147 (2014) 1–22.
[52] P. Beard, Biomedical photoacoustic imaging, Interface Focus 1 (2011) 602–631.
[53] J.I. Korenbrot, Speed, sensitivity, and stability of the light response in rod and cone photoreceptors: facts and models, Prog. Retin. Eye Res. 31 (2012) 442–466.
[54] C. Pierrot-Deseilligny, D. Milea, R.M. Müri, Eye movement control by the cerebral cortex, Curr. Opin. Neurol. 17 (2004) 17–25.
[55] F.C. Delori, R.H. Webb, D.H. Sliney, Maximum permissible exposures for ocular safety (ANSI 2000), with emphasis on ophthalmic devices, J. Opt. Soc. Am. A Opt. Image Sci. Vis. 24 (2007) 1250–1265.
[56] D.T. Organisciak, D.K. Vaughan, Retinal light damage: mechanisms and protection, Prog. Retin. Eye Res. 29 (2010) 113–134.
[57] Guidelines on limits of exposure to broad-band incoherent optical radiation (0.38 to 3 microM). International Commission on Non-Ionizing Radiation Protection, Health Phys. 73 (1997) 539–554.
[58] American National Standard for safe use of lasers, ANSI 136.1 (2014).
[59] D.A. Robinson, The mechanics of human saccadic eye movement, J. Physiol. 174 (1964) 245–264.
[60] D. Schweitzer, E. Thamm, M. Hammer, J. Kraft, A new method for the measurement of oxygen saturation at the human ocular fundus, Int. Ophthalmol. 23 (2001) 347–353.
[61] P.E. Kilbride, K.R. Alexander, M. Fishman, G.A. Fishman, Human macular pigment assessed by imaging fundus reflectometry, Vis. Res. 29 (1989) 663–674.
[62] M. Hammer, D. Schweitzer, Quantitative reflection spectroscopy at the human ocular fundus, Phys. Med. Biol. 47 (2002) 179–191.
[63] A. de la Zerda, Y.M. Paulus, R. Teed, S. Bodapati, Y. Dollberg, B.T. Khuri-Yakub, M.S. Blumenkranz, D.M. Moshfeghi, S.S. Gambhir, Photoacoustic ocular imaging, Opt. Lett. 35 (2010) 270–272.
[64] S. Hu, B. Rao, K. Maslov, L.V. Wang, Label-free photoacoustic ophthalmic angiography, Opt. Lett. 35 (2010) 1–3.
[65] S. Jiao, M. Jiang, J. Hu, A. Fawzi, Q. Zhou, K.K. Shung, C.A. Puliafito, H.F. Zhang, Photoacoustic ophthalmoscopy for in vivo retinal imaging, Opt. Express 18 (2010) 3967–3972.
[66] W. Xing, L. Wang, K. Maslov, L.V. Wang, Integrated optical- and acoustic-resolution photoacoustic microscopy based on an optical fiber bundle, Opt. Lett. 38 (2013) 52–54.
[67] K. Maslov, G. Stoica, L.V. Wang, In vivo dark-field reflection-mode photoacoustic microscopy, Opt. Lett. 30 (2005) 625–627.
[68] K. Maslov, H.F. Zhang, S. Hu, L.V. Wang, Optical-resolution photoacoustic microscopy for in vivo imaging of single capillaries, Opt. Lett. 33 (2008) 929–931.
[69] W. Song, Q. Wei, T. Liu, D. Kuai, J.M. Burke, S. Jiao, H.F. Zhang, Integrating photoacoustic ophthalmoscopy with scanning laser ophthalmoscopy optical coherence tomography, and fluorescein angiography for a multimodal retinal imaging platform, J. Biomed. Opt. 17 (2012) 0612061–0612067.
[70] S.N. Hennen, W. Xing, Y.-B. Shui, Y. Zhou, J. Kalishman, L.B. Andrews-Kaminsky, M.A. Kass, D.C. Beebe, K.I. Maslov, L.V. Wang, Photoacoustic tomography imaging and estimation of oxygen saturation of hemoglobin in ocular tissue of rabbits, Exp. Eye Res. (2015) 1–6.
[71] W. Song, Q. Wei, W. Liu, T. Liu, J. Yi, N. Sheibani, A.A. Fawzi, R.A. Linsenmeier, S. Jiao, H.F. Zhang, A combined method to quantify the retinal metabolic rate of oxygen using photoacoustic ophthalmoscopy and optical coherence tomography, Sci. Rep. 4 (2014) 6525.
[72] R.H. Silverman, F. Kong, Y.C. Chen, H.O. Lloyd, H.H. Kim, J.M. Cannata, K.K. Shung, D.J. Coleman, High-resolution photoacoustic imaging of ocular tissues, Ultrasound Med. Biol. 36 (2010) 733–742.
[73] W. Liu, K.M. Schultz, K. Zhang, A. Sasman, F. Gao, T. Kume, H.F. Zhang, In vivo corneal neovascularization imaging by optical-resolution photoacoustic microscopy, Photoacoustics 2 (2014) 81–86.
[74] N. Wu, S. Ye, Q. Ren, C. Li, High-resolution dual-modality photoacoustic ocular imaging, Opt. Lett. 39 (2014) 2451–2454.
[75] J.M. Thijssen, H.J.M. Mol, M.J.T.M. Cloostermans, W.J.M. Verhoef, M. Van Lieshout, M.R. Timmer, A.M. Verbeek, Acoustic parameters of ocular tissues, in: J. Hillman, M. Le May (Eds.), Ophthalmic Ultrasonography, Springer, Netherlands, 1983, pp. 445–450.
[76] W. Song, Q. Wei, L. Feng, V. Sarthy, S. Jiao, X. Liu, H.F. Zhang, Multimodal photoacoustic ophthalmoscopy in mouse, J. Biophoton. 6 (2013) 505–512.
[77] T. Liu, H. Li, W. Song, S. Jiao, H.F. Zhang, Fundus camera guided photoacoustic ophthalmoscopy, Curr. Eye Res. 38 (2013) 1229–1234.
[78] Q. Wei, T. Liu, S. Jiao, H.F. Zhang, Image chorioretinal vasculature in albino rats using photoacoustic ophthalmoscopy, J. Mod. Optic. 58 (2011) 1997–2001.
[79] X. Liu, T. Liu, R. Wen, Y. Li, C.A. Puliafito, H.F. Zhang, S. Jiao, Optical coherence photoacoustic microscopy for in vivo multimodal retinal imaging, Opt. Lett. 40 (2015) 1370–1373.
[80] T. Liu, Q. Wei, W. Song, J.M. Burke, S. Jiao, H.F. Zhang, Near-infrared light photoacoustic ophthalmoscopy, Biomed. Opt. Express 3 (2012) 792–799.
[81] W. Song, Q. Wei, R. Zhang, H.F. Zhang, In vivo photoacoustic chorioretinal vascular imaging in albino mouse, Chin. Opt. Lett. 12 (2014) 051704.
[82] R. Bernardes, C. Lobo, J.G. Cunha-Vaz, Multimodal macula mapping: a new approach to study diseases of the macula, Surv. Ophthalmol. 47 (2002) 580–589.
[83] R. Forte, G. Querques, L. Querques, N. Massamba, V. Le Tien, E.H. Souied, Multimodal imaging of dry age-related macular degeneration, Acta Ophthalmol. (Copenh.) 90 (2012) e281–e287.
[84] E.J. Fernandez, B. Hermann, B. Povazay, A. Unterhuber, H. Sattmann, B. Hofer, P.K. Ahnelt, W. Drexler, Ultrahigh resolution optical coherence tomography and pancorrection for cellular imaging of the living human retina, Opt. Express 16 (2008) 11083–11094.
[85] J.G. Fujimoto, Optical coherence tomography for ultrahigh resolution in vivo imaging, Nat. Biotechnol. 21 (2003) 1361–1367.
[86] Y. Jia, O. Tan, J. Tokayer, B. Potsaid, Y. Wang, J.J. Liu, M.F. Kraus, H. Subhash, J.G. Fujimoto, J. Hornegger, D. Huang, Split-spectrum amplitude-decorrelation angiography with optical coherence tomography, Opt. Express 20 (2012) 4710–4725.
[87] Y. Jia, S.T. Bailey, T.S. Hwang, S.M. McClintic, S.S. Gao, M.E. Pennesi, C.J. Flaxel, A.K. Lauer, D.J. Wilson, J. Hornegger, J.G. Fujimoto, D. Huang, tative optical coherence tomography angiography of vascular abnormalities in the living human, Proc Natl. Acad. Sci. U. S. A. 112 (2015) E2395–E2402.
[88] W. Liu, H. Li, R.S. Shah, X. Shu, R.A. Linsenmeier, A.A. Fawzi, H.F. Zhang, Simultaneous optical coherence tomography angiography and fluorescein angiography in rodents with normal retina and laser-induced choroidal neovascularization, Opt. Lett. 40 (2015) 5782–5785.
[89] R.A. Leitgeb, R.M. Werkmeister, C. Blatter, L. Schmetterer, Doppler optical coherence tomography, Prog. Retin. Eye Res. 41 (2014) 26–43.
[90] W. Liu, J. Yi, S. Chen, S. Jiao, H.F. Zhang, Measuring retinal blood flow in rats using doppler optical coherence tomography without knowing eyeball axial length, Med. Phys. 42 (2015) 5356–5362.
[91] O. Tan, R. Konduru, X. Zhang, S.R. Sadda, D. Huang, Dual-angle protocol for doppler optical coherence tomography to improve retinal blood flow measurement, Transl. Vis. Sci. Technol. 3 (2014) 6–6.
[92] B. Baumann, W. Choi, B. Potsaid, D. Huang, J.S. Duker, J.G. Fujimoto, Swept source/Fourier domain polarization sensitive optical coherence tomography with a passive polarization delay unit, Opt. Express 20 (2012) 10229–10241.
[93] M. Pircher, C.K. Hitzenberger, U. Schmidt-Erfurth, Polarization sensitive optical coherence tomography in the human eye, Prog. Retin. Eye Res. 30 (2011) 431–451.
[94] M.J. Ju, Y.-J. Hong, S. Makita, Y. Lim, K. Kurokawa, L. Duan, M. Miura, S. Tang, Y. Yasuno, Advanced multi-contrast Jones matrix optical coherence tomography for Doppler and polarization sensitive imaging, Opt. Express 21 (2013) 19412–19436.
[95] H.F. Zhang, C.A. Puliafito, S. Jiao, Photoacoustic ophthalmoscopy for in vivo retinal imaging: current status and prospects, Ophthal. Surg. Lasers Imaging 42 (2011) S106–S115.
[96] X. Zhang, H.F. Zhang, C.A. Puliafito, S. Jiao, Simultaneous in vivo imaging of melanin and lipofuscin in the retina with photoacoustic ophthalmoscopy and autofluorescence imaging, J. Biomed. Opt. 16 (2011) (080504-080504-080503).
[97] W. Liu, H.F. Zhang, Noninvasive in vivo imaging of oxygen metabolic rate in the retina, Conf. Proc. IEEE Eng. Med. Biol. Soc. 2014 (2014) 3865–3868.
[98] H. Li, B. Dong, Z. Zhang, H.F. Zhang, C. Sun, A transparent broadband ultrasonic detector based on an optical micro-ring resonator for photoacoustic microscopy, Sci. Rep. 4 (2014) 4496.
[99] B. Dong, H. Li, Z. Zhang, K. Zhang, S. Chen, C. Sun, H.F. Zhang, Isometric multimodal photoacoustic microscopy based on optically transparent micro-ring ultrasonic detection, Optica 2 (2015) 169–176.
[100] B. Dong, S. Chen, Z. Zhang, C. Sun, H.F. Zhang, Photoacoustic probe using a microring resonator ultrasonic sensor for endoscopic applications, Opt. Lett. 39 (2014) 4372–4375.
[101] R.W. Speirs, A.I. Bishop, Photoacoustic tomography using a Michelson interferometer with quadrature phase detection, Appl. Phys. Lett. 103 (2013) 053501.
[102] Y. Wang, C. Li, R.K. Wang, Noncontact photoacoustic imaging achieved by using a low-coherence interferometer as the acoustic detector, Opt. Lett. 36 (2011) 3975–3977.
[103] B.P. Payne, V. Venugopalan, B.B. Mikic, N.S. Nishioka, Optoacoustic tomography using time-resolved interferometric detection of surface displacement, J. Biomed. Opt. 8 (2003) 273–280.
[104] G. Rousseau, A. Blouin, J.-P. Monchalin, Non-contact photoacoustic tomography and ultrasonography for tissue imaging, Biomed. Opt. Express 3 (2012) 16–25.

[105] A. Hochreiner, J. Bauer-Marschallinger, P. Burgholzer, B. Jakoby, T. Berer, Non-contact photoacoustic imaging using a fiber based interferometer with optical amplification, Biomed. Opt. Express 4 (2013) 2322–2331.
[106] A. Sampathkumar, R.H. Silverman, Non-contact photoacoustic characterization of retinal vasculature for brain-injury assessment, Ultrasonics Symposium (IUS), 2014 IEEE International (2014) 843–845.
[107] Z. Chen, S. Yang, Y. Wang, D. Xing, All-optically integrated photo-acoustic microscopy and optical coherence tomography based on a single Michelson detector, Opt. Lett. 40 (2015) 2838–2841.
[108] C. Lee, S. Han, S. Kim, M. Jeon, M.Y. Jeon, C. Kim, J. Kim, Combined photoacoustic and optical coherence tomography using a single near-infrared supercontinuum laser source, Appl. Opt. 52 (2013) 1824–1828.
[109] X. Liu, T. Liu, R. Wen, Y. Li, C.A. Puliafito, H.F. Zhang, S. Jiao, Optical coherence photoacoustic microscopy for in vivo multimodal retinal imaging, Opt. Lett. 40 (2015) 1370–1373.
[110] R.G. Kolkman, W. Steenbergen, T.G. van Leeuwen, In vivo photoacoustic imaging of blood vessels with a pulsed laser diode, Lasers Med. Sci. 21 (2006) 134–139.
[111] T. Wang, S. Nandy, H.S. Salehi, P.D. Kumavor, Q. Zhu, A low-cost photoacoustic microscopy system with a laser diode excitation, Biomed. Opt. Express 5 (2014) 3053–3058.
[112] Y. Zhou, J. Yao, L.V. Wang, Optical clearing-aided photoacoustic microscopy with enhanced resolution and imaging depth, Opt. Lett. 38 (2013) 2592–2595.
[113] P. Hai, J. Yao, K.I. Maslov, Y. Zhou, L.V. Wang, Near-infrared optical-resolution photoacoustic microscopy, Opt. Lett. 39 (2014) 5192–5195.
[114] M.L. Li, H.E. Zhang, K. Maslov, G. Stoica, L.V. Wang, Improved in vivo photoacoustic microscopy based on a virtual-detector concept, Opt. Lett. 31 (2006) 474–476.
[115] N.D. Shemonski, F.A. South, Y.Z. Liu, S.G. Adie, P.S. Carney, S.A. Boppart, Computational high-resolution optical imaging of the living human retina, Nat. Photon. 9 (2015) 440–443.
[116] T. Ma, X. Zhang, C.T. Chiu, R. Chen, K. Kirk Shung, Q. Zhou, S. Jiao, Systematic study of high-frequency ultrasonic transducer design for laser-scanning photoacoustic ophthalmoscopy, J. Biomed. Opt. 19 (2014) 16015.
[117] G.P. Luke, D. Yeager, S.Y. Emelianov, Biomedical applications of photoacoustic imaging with exogenous contrast agents, Ann. Biomed. Eng. 40 (2012) 422–437.
[118] W. Li, X. Chen, Gold nanoparticles for photoacoustic imaging, Nanomedicine (London, England) 10 (2015) 299–320.
[119] H. Radhakrishnan, V.J. Srinivasan, Multiparametric optical coherence tomography imaging of the inner retinal hemodynamic response to visual stimulation, J. Biomed. Opt. 18 (2013) 086010–086010.
[120] C.E. Riva, E. Logean, B. Falsini, Visually evoked hemodynamical response and assessment of neurovascular coupling in the optic nerve and retina, Prog. Retin. Eye Res. 24 (2005) 183–215.
[121] M. Hammer, W. Vilser, T. Riemer, F. Liemt, S. Jentsch, J. Dawczynski, D. Schweitzer, Retinal venous oxygen saturation increases by flicker light stimulation, Invest. Ophthalmol. Vis. Sci. 52 (2011) 274–277.
[122] K. Polak, L. Schmetterer, C.E. Riva, Influence of flicker frequency on flicker-induced changes of retinal vessel diameter, Invest. Ophthalmol. Vis. Sci. 43 (2002) 2721–2726.
[123] J. Kim, W. Brown, J.R. Maher, H. Levinson, A. Wax, Functional optical coherence tomography: principles and progress, Phys. Med. Biol. 60 (2015) R211–237.
[124] T.E. de Carlo, A. Romano, N.K. Waheed, J.S. Duker, A review of optical coherence tomography angiography (OCTA), Int. J. Retina Vitreous 1 (2015) 1–15.
[125] J. Yi, W. Liu, S. Chen, V. Backman, N. Sheibani, C.M. Sorenson, A.A. Fawzi, R.A. Linsenmeier, H.F. Zhang, Visible light optical coherence tomography measures retinal oxygen metabolic response to systemic oxygenation, Light Sci. Appl. 4 (2015).
[126] P.F. Sharp, A. Manivannan, H. Xu, J.V. Forrester, The scanning laser ophthalmoscope–a review of its role in bioscience and medicine, Phys. Med. Biol. 49 (2004) 1085–1096.
[127] B.I. Gramatikov, Modern technologies for retinal scanning and imaging: an introduction for the biomedical engineer, Biomed Eng. Online 13 (2014) 52.
[128] R. Bernardes, P. Serranho, C. Lobo, Digital ocular fundus imaging: a review, Ophthalmologica 226 (2011) 161–181.
[129] H. Li, W. Liu, H.F. Zhang, Investigating the influence of chromatic aberration and optical illumination bandwidth on fundus imaging in rats, J. Biomed. Opt. 20 (2015) 106010.
[130] V. Nourrit, J. Denniss, M.M. Muqit, I. Schiessl, C. Fenerty, P.E. Stanga, D.B. Henson, High-resolution hyperspectral imaging of the retina with a modified fundus camera, J. Fr. Ophtalmol. 33 (2010) 686–692.
[131] S.R. Patel, J.G. Flanagan, A.M. Shahidi, J.-P. Sylvestre, C. Hudson, A prototype hyperspectral system with a tunable laser source for retinal vessel imaginga prototype hyperspectral system, Invest. Ophthalmol. Vis. Sci. 54 (2013) 5163–5168.
[132] J. Yao, K. Maslov, S. Hu, L.V. Wang, Evans blue dye-enhanced capillary-resolution photoacoustic microscopy in vivo, J. Biomed. Opt. 14 (2009) 054049.
[133] G. Kim, S.W. Huang, K.C. Day, M. O'Donnell, R.R. Agayan, M.A. Day, R. Kopelman, S. Ashkenazi, Indocyanine-green-embedded PEBBLEs as a contrast agent for photoacoustic imaging, J. Biomed. Opt. 12 (2007) 044020.
[134] S. Zanganeh, H. Li, P.D. Kumavor, U. Alqasemi, A. Aguirre, I. Mohammad, C. Stanford, M.B. Smith, Q. Zhu, Photoacoustic imaging enhanced by indocyanine green-conjugated single-wall carbon nanotubes, J. Biomed. Opt. 18 (2013) 096006.
[135] X. Yang, E.W. Stein, S. Ashkenazi, L.V. Wang, Nanoparticles for photoacoustic imaging, Wiley Interdiscip. Rev.: Nanomed. Nanobiotechnol. 1 (2009) 360–368.

Wenzhong Liu completed his B.S. in Biomedical Engineering from Tian Jin University, Tian Jin, China in 2008, and earned his M.S. in Biomedical Engineering from Shanghai Jiao Tong University, Shanghai, China in 2011. He is currently a Ph.D. candidate and a HHMI International Student Research Fellow in the Department of Biomedical Engineering at Northwestern University. He is interested in functional imaging of the eye.

Hao F. Zhang received his Ph.D. in Biomedical Engineering from Texas A&M University, College Station, TX in 2006. From 2006 to 2007, he was a post-doctoral fellow at Washington University in St. Louis, St. Louis, MO. He is currently an Associate Professor in the Department of Biomedical Engineering and Department of Ophthalmology at Northwestern University, Evanston, IL. His research interests include optical microscopy, nonlinear optics, laser-tissue interaction, retinal imaging, and image processing.